Single-Atom MnN$_5$ Catalytic Sites Enable Efficient Peroxymonosulfate Activation by Forming Highly Reactive Mn(IV)−Oxo Species

Jie Miao, Jian Song, Junyu Lang, Yuan Zhu, Jie Dai, Yan Wei, Mingce Long,* Zongping Shao, Baoxue Zhou, Pedro J. J. Alvarez, and Lizhi Zhang*

ACCESS | Metrics & More | Article Recommendations | Supporting Information

ABSTRACT: Four-nitrogen-coordinated transition metal (MN$_4$) configurations in single-atom catalysts (SACs) are broadly recognized as the most efficient active sites in peroxymonosulfate (PMS)-based advanced oxidation processes. However, SACs with a coordination number higher than four are rarely explored, which represents a fundamental missed opportunity for coordination chemistry to boost PMS activation and degradation of recalcitrant organic pollutants. We experimentally and theoretically demonstrate here that five-nitrogen-coordinated Mn (MnN$_5$) sites more effectively activate PMS than MnN$_4$ sites, by facilitating the cleavage of the O−O bond into high-valent Mn(IV)−oxo species with nearly 100% selectivity. The high activity of MnN$_5$ was discerned to be due to the formation of higher-spin-state N$_5$Mn(IV)=O species, which enable efficient two-electron transfer from organics to Mn sites through a lower-energy-barrier pathway. Overall, this work demonstrates the importance of high coordination numbers in SACs for efficient PMS activation and informs the design of next-generation environmental catalysts.

KEYWORDS: peroxymonosulfate activation, single-atom catalysts, coordination number, high-valent Mn(IV)−oxo species, high-spin state
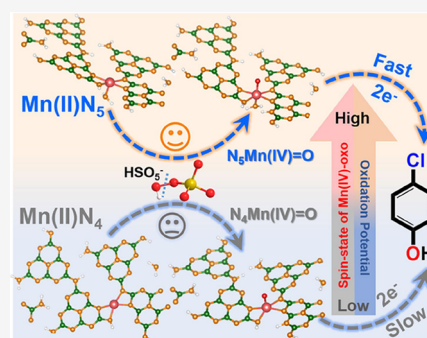
INTRODUCTION

Heterogeneous peroxymonosulfate (PMS)-based advanced oxidation processes (AOPs) are powerful remediation technologies to treat recalcitrant organic contaminants in water.[1−4] Catalysts with transition metals are efficient persulfate activators to produce free radicals (e.g., SO$_4^{·-}$) that oxidize the target pollutants,[5−7] but these radicals suffer from scavenging by background constituents and ultrashort lifetimes (10^{-6}–10^{-9} s),[8,9] which hinders their efficacy in complex matrices. High-valent metal−oxo (HVMO) species, as typical nonradical oxidative species generated in persulfate activation, are promising candidates for water purification, owing to their much longer lifetime (e.g., 7−10 s for Fe(IV)=O), higher steady-state concentrations ($\sim 10^{-9} \gg 10^{-12}$–$10^{-15}$ M for radicals), ultrahigh oxidant utilization efficiency, and selective reactivity toward organics.[8,10−13] However, HVMO species are usually generated in homogeneous systems catalyzed by transition metals that also produce other reactive species (e.g., $^·$OH and ^{1}O$_2$),[14−17] and this decreases the utilization efficiency of the oxidant (e.g., PMS).[18,19] Therefore, it is important to develop transition metal-based heterogeneous catalysts that activate persulfate by efficiently generating HVMO species with high reactivity.

Single-atom catalysts (SACs) have emerged as promising heterogeneous catalysts for PMS activation due to their utmost atom utilization efficiency and high selectivity for diverse catalytic reactions.[1,20−23] Especially, four-nitrogen coordinated SACs display significantly high selectivity in HVMO generation during PMS activation.[1,8,24] For example, electron-depleted CuN$_4$/C−B was reported to boost PMS activation and form Cu(III)−OH reactive species for bisphenol A removal.[1] Also, Fe(IV)−HVMO was found to be the major oxidizing species in FeN$_4$ single-site catalyzed PMS activation, and it exhibited selective reactivity for oxidizing organic contaminants of emerging concern.[8]

The coordination number of M−N moieties in SACs strongly affects the geometric and electronic properties, as well as the catalytic activity of SACs. While SACs with a coordination number higher than four have been used for selective conversion of hydrocarbons and oxygen reduction reactions[25−27] and play prominent roles in biomimetic and enzymatic oxidation reactions,[28−30] the five-nitrogen coordinated SACs are seldom explored for persulfate activation

except for Fe−N$_5$ SACs.[31,32] This represents a fundamental knowledge gap and a missed opportunity for coordination chemistry using other transition metal SACs (such as Co, Mn, Cu, and Ni) to boost PMS activation and enhance the degradation of recalcitrant organic pollutants. For instance, while Mn SACs have been tested for HVMO-dominated persulfate activation, five-nitrogen coordinated Mn SACs have not. Herein, we experimentally and theoretically investigated the five-nitrogen coordinated Mn configuration (MnN$_5$) in PMS activation via the Mn−HVMO pathway. We also synthesized g-C$_3$N$_4$-supported MnN$_5$ to demonstrate the importance of high coordination numbers in SACs for efficient PMS activation and discerned how the high coordination number of Mn−N moieties enhances PMS-based AOPs to inform the design of next-generation catalysts.

■ EXPERIMENTAL SECTION

Materials. Dicyandiamide (DCD), manganese(III) acetylacetonate (Mn(acac)$_3$), ammonium chloride (NH$_4$Cl), 2,2′-azino-bis(3-ethylbenzothiazoline-6-sulfonic acid)diammonium salt (ABTS), PMS, and 2,2,6,6-tetramethylpiperidine (TEMP) were purchased from Sigma-Aldrich Chemical Co., Ltd. Methanol (MeOH), p-chlorophenol (4-CP), and furfuryl alcohol (FFA) were obtained from Sinopharm Chemical Reagent Co., Ltd.

Synthesis of g-C$_3$N$_4$. Graphitic carbon nitride (g-C$_3$N$_4$, CN) was prepared by using DCD as the precursor. Typically, 5.0 g of DCD was heated to 550 °C with a rate of 2.5 °C/min and kept for 4 h in a muffle furnace. After cooling to room temperature, the yellow residual was grinded to obtain g-C$_3$N$_4$.

Synthesis of Mn SACs. For the synthesis of MnN$_5$, NH$_4$Cl was selected to control the coordination environment of Mn single-atom sites on g-C$_3$N$_4$. Typically, 0.5 g of g-C$_3$N$_4$ and 0.25 mmol of Mn(acac)$_3$ were mixed with 8 mmol NH$_4$Cl molar weight in a mortar and thoroughly grinded. Then, the obtained sample was heated to 550 °C with a rate of 2.5 °C/min under an Ar atmosphere for 4 h in a tube furnace. Finally, the products were washed with ultrapure water to remove soluble Mn salts, dried at 60 °C for 12 h, and collected after grinding to obtain MnN$_5$. A series of samples MnN$_5$-x (x = 1, 2, and 3) were obtained corresponding to 4, 8, and 12 mmol NH$_4$Cl molar weight, respectively. If not specified, MnN$_5$-2 (labeled as MnN$_5$) was used in most of the investigations due to its optimal performance. MnN$_4$ was synthesized by a similar procedure but without the addition of NH$_4$Cl.

Characterization. The crystal phases and morphologies of catalysts were determined by Rigaku D/max-2200/PC X-ray diffraction (XRD) and TECNA1 G2F20 transmission electron microscopy (TEM), respectively. N$_2$ adsorption−desorption isotherms were recorded on a Nova 2200e gas sorption analyzer (Quantachrome Instruments). High-angle annular dark-field scanning transmission electron microscopy (HAADF-STEM) was conducted on a JEOL JEM-ARF200F atom resolution analytical microscope. X-ray photoelectron spectroscopy (XPS) analyses were performed on an Axis Ultra DLD system (Shimadzu/Kratos). Raman spectra were recorded on a Bruker Senterra R200-L dispersive Raman microscope at 532 nm. Zero-field-cooled (ZFC) and field-cooled (FC) measurements were executed by a magnetic property measurement system (MPMS, Quantum Design) under H = 1 kOe for temperature-dependent (2−400 K) magnetization measurements. The Mn contents in MnN$_5$-x catalysts were measured by an inductively coupled plasma mass

spectrometer (Thermo Fisher Scientific). The X-ray absorption experiments were carried out at the XAS (X-ray absorption spectra) station (BL14W1) of the Shanghai Synchrotron Radiation Facility (SSRF). The electron storage ring was operated at 3.5 GeV. Si(311) double-crystal was used as the monochromator, and the data were collected using a solid-state detector under ambient conditions. The beam size was limited by the horizontal and vertical slits with an area of 1 × 4 mm^2 during XAS measurements. The X-ray absorption of a Mn foil at Mn K-edge was measured for energy calibration. The spectra analysis and fitting were processed by the software codes of Artemis and Athena.

DFT Calculations. All spin-polarized periodic calculations were carried out using the Vienna Ab initio Simulation Package (VASP). The remaining core electrons were described by the projector augmented-wave method. The 2s and 2p electrons in carbon, oxygen, sulfur, and nitrogen and the 3p, 3d, and 4s electrons in manganese were treated as valence electrons. The kinetic cut-off energy was set to 450 eV for all calculations. The surface models of MnN$_4$ and MnN$_5$ were built on g-C$_3$N$_4$ with a vacuum layer of 15 Å to avoid the interaction between contiguous period layers. The Monkhorst−Pack k-point mesh was set to 3 × 4 × 1 for both the surface and adsorbed models. The energy change and force convergence tolerance were chosen to be less than 10^{-5} eV atom^{-1} and 0.02 eV Å^{-1}, respectively.

The Gibbs free energy is calculated using eq 1, where ΔE^*, ΔE_{ZPE}, and ΔS represent the adsorption energy, zero-point energy variation, and entropy variation, respectively. Zero-point energy was obtained by the vibrational frequency calculation with a selective dynamics method because the vibrational contribution of MnN$_4$ and MnN$_5$ surfaces can be neglected in this process.

$$\Delta G^* = \Delta E^* + \Delta E_{ZPE} - T\Delta S \tag{1}$$

Catalytic Performance. The tests of 4-CP removal (10 mg L^{-1}, 50 mL) in the activated PMS process were performed in a beaker. Around 25 mg of Mn SACs were first dispersed into the 4-CP solution and stirred for 30 min to reach adsorption−desorption equilibrium. Then, 15.4 mg of PMS was added to initiate the catalytic degradation process. An appropriate amount of the aqueous solution was taken at a given time interval, and the concentration of residual 4-CP was analyzed by high-performance liquid chromatography (Shimadzu LC-2010AHT). Residual PMS in the solution was detected by a reported ABTS method.[33] The reactive oxygen species (ROS) in PMS activation systems were identified by a Bruker microEPR spectrometer. In the recycle tests, MnN$_5$ was collected after the reaction, and regenerated via elution with MeOH to thoroughly remove the adsorbed organic intermediates, and dried before the next run.

■ RESULTS AND DISCUSSION

Synthesis and Characterization of MnN$_5$ SACs. Graphitic carbon nitride, with the well-defined tri-s-triazine framework, is frequently used as the support for isolated metal sites by calcining a mixture of metal sources and DCD, and this often produces MN$_4$ due to the formation of four-nitrogen coordinated precursors.[34] To increase nitrogen coordination numbers, we introduced an external nitrogen source (NH$_4$Cl) during the CN-based synthesis process because the decomposition of NH$_4$Cl at temperatures above 520 °C generates
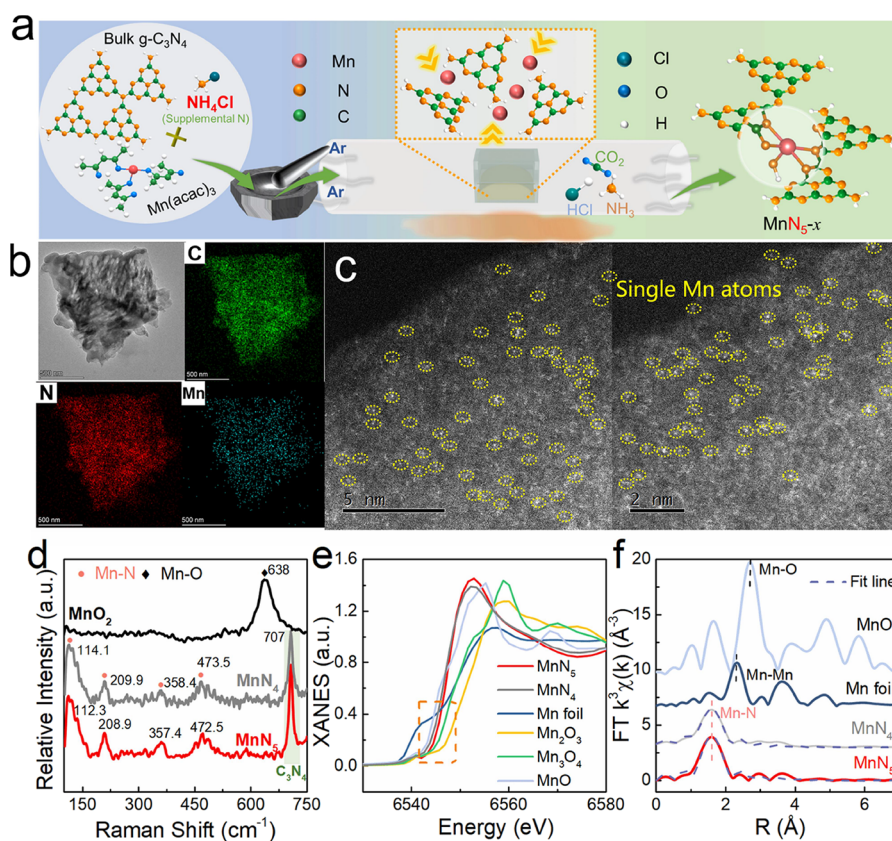
Figure 1. Preparation, morphology, and coordination environment characterization of MnN_5 SACs. (a) Schematic procedure for the synthesis of MnN_5; (b) EDS-mapping images and (c) HAADF-STEM images of MnN_5; (d) Raman spectra of MnO_2, MnN_4, and MnN_5; and (e) Mn K-edge XANES spectra and (f) FT-EXAFS spectra of different samples.

gaseous HCl and NH_3. HCl induces delamination and disintegration of bulk g-C_3N_4, while NH_3 enables amino groups' anchoring on the metal sites to form extra coordinated structures.[35] Figure 1a illustrates the NH_4Cl-mediated calcination approach to synthesize Mn SACs with a five-nitrogen coordination structure (MnN_5). MnN_5 with different nitrogen contents (MnN_5-x, x = 1–3) was synthesized by varying the NH_4Cl doses (Table S1). The CN (NH_4Cl) and MnN_4 control samples were also synthesized by a similar procedure without a Mn precursor and NH_4Cl addition, respectively.

As shown by TEM images (Figures 1b and S1, S2), MnN_4 and MnN_5 displayed a lamellar structure, without visible nanoparticles. Only typical diffraction peaks of g-C_3N_4 appeared in the XRD patterns of Mn SACs (Figure S3), ruling out the formation of Mn chlorides or Mn oxides.[36,37] The absence of Mn chlorides was further proved by XPS measurements (Figure S4a), in which no Cl signal was detected on all catalysts. The atomically dispersive Mn species over the support of g-C_3N_4 was evidenced by the HAADF-STEM equipped with a probe aberration corrector according to the bright spots of atomic scale (Figures 1c and S5). The element mapping images in Figure 1b further identified the uniform distribution of Mn atoms in the entire CN support. Furthermore, the mass content of Mn was comparable in all samples (2.7–3.0 wt %, measured by inductively coupled plasma atomic emission spectroscopy) (Table S2).

The structure of Mn−N coordination in MnN_4 and MnN_5 was proved by Raman spectra (Figure 1d). It displays no Mn−O coordination peak but new peaks at ∼208.9, 357.4, and

472.5 cm^{-1}, which are attributed to the stretching or deformation vibration of out-of-plane Mn−N modes, further identifying the existence of Mn−N bonds in both catalysts.[36,38] The downward shift of N 1s XPS binding energies in Mn SACs (Figure S6) in comparison to pristine CN provided further indication of the changes of nitrogen bonding structures.[34,39] In comparison with CN, there was no evidence of Mn−C and Mn−O species in C 1s (Figure S7) and O 1s (Figure S8) XPS spectra of Mn SACs, unambiguously suggesting the formation of Mn−N coordination structures. The fine structures of Mn−N moieties in MnN_4 and MnN_5 were then compared by synchrotron X-ray absorption spectra. The Mn K-edge X-ray absorption near-edge structure (XANES) spectra (Figure 1e) show that the rising edges of the normalized K-edge for both catalysts are located much closer to that of MnO than that of Mn_3O_4, suggesting that Mn atoms are in an oxidation state with an average valence of about +2. This agrees with the XPS results, showing a distinct shake-up satellite peak of Mn^{2+} at 646.0 eV (Figure S9). The Fourier transform extended X-ray absorption fine structure (FT-EXAFS) spectra of MnN_5 (Figure 1f) had a solitary peak for the Mn−N shell at about 1.65 Å, which is similar to that of MnN_4 (Figure 1f) but significantly different from that of the Mn−Mn bond (Mn foil) at ∼2.33 Å and the Mn−O bond (MnO) at ∼2.72 Å, verifying atomically dispersed Mn−N moieties in both Mn SACs. The coordination number of Mn−N was calculated to be 5.19 ± 0.33 for MnN_5, significantly higher than that of MnN_4 (4.34 ± 0.28) (Figure S10a,b and Table S3), inferring that the isolated Mn atoms were 4- and 5-fold coordinated by N atoms in MnN_4 and MnN_5, respectively.
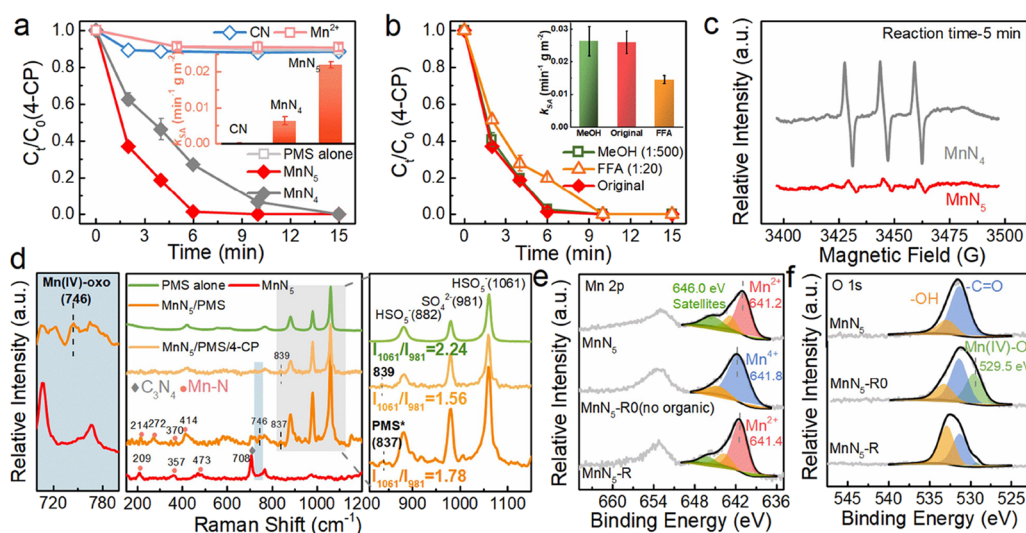
Figure 2. Removal of 4-CP and proof of a nonradical mechanism in Mn SAC/PMS systems. (a) Degradation profiles of 4-CP in CN (NH$_4$Cl)/PMS, Mn^{2+}/PMS, and different Mn SAC/PMS systems; inset: comparison of the specific activity (k_{SA}) of the catalysts. (b) Effect of scavengers on 4-CP degradation in the MnN$_5$/PMS system. (c) EPR spectra for singlet oxygen in the MnN$_4$/PMS and MnN$_5$/PMS systems. (d) In situ Raman spectra. (e) Mn 2p XPS spectra and (f) O 1s XPS spectra of MnN$_5$, MnN$_5$/PMS (MnN$_5$-R0), and MnN$_5$/PMS/4-CP (MnN$_5$-R). Reaction conditions: [4-CP]$_0$ = 10 mg L^{-1}, [catalyst] = 0.5 g L^{-1}, [PMS]$_0$ = 1.0 mM, pH$_{initial}$ = 6.7, and T = 25 °C.

PMS Activation over MnN$_5$ Proceeded through a Mn(IV)−Oxo Dominated Pathway. The effect of nitrogen coordination numbers of Mn SACs on PMS activation activity was examined via degradation of 4-CP, a common recalcitrant organic pollutant. Before comparing the catalytic performances of these Mn SACs, the effect of the catalyst concentration on PMS activation was explored, as observed in Figure S11, thus determining an optimal catalyst dosage of 0.5 g L^{-1}. As shown in Figure 2a, almost 100% 4-CP (10 mg/L) was removed by adding MnN$_5$ and PMS (MnN$_5$/PMS) in 6 min, much faster than that with MnN$_4$ and PMS (73% removal). CN (NH$_4$Cl) and homogeneous Mn(II) ions (0.5 g L^{-1}, much higher than the Mn leaching contents listed in Table S4) exhibited very poor activity for PMS activation (less than 10% 4-CP removal) (Figure 2a), and all Mn SACs resulted in negligible 4-CP adsorption (Figure S12). The specific apparent rate constants (k_{SA}, min^{-1} g m^{-2}) (Figure S13) were calculated by normalizing the observed pseudo-first-order kinetic constants (k_{obs}) by their specific surface areas (SSAs) (Table S2 and Figure S14). The k_{SA} value of MnN$_5$ (0.022 min^{-1} g m^{-2}) was highest (inset of Figure 2a), 110- and 3.7-fold higher than that of g-C$_3$N$_4$ (0.0002 min^{-1} g m^{-2}) and MnN$_4$ (0.006 min^{-1} g m^{-2}), respectively. The intrinsic catalytic performance of MnN$_5$ was superior to that of many reported Mn-based catalysts and Cu/Fe SACs (Figure S15 and Table S5).[1,21,40−45] More importantly, MnN$_5$ still retained high activity after six successive catalytic recycles (Figure S16), implying its long-term stability. MnN$_5$ was also more active than MnN$_4$ to remove various refractory pollutants via efficient PMS activation, including phenol, bisphenol A, sulfathiazole, and sulfamethoxazole (Figure S17). Furthermore, although the initial pH of the reaction solution changed from 3.5 to 10.5, the pH had a negligible influence on 4-CP removal in the MnN$_5$/PMS system (Figure S18a). The highly effective catalytic performance of MnN$_5$ was also observed in the complex water matrices (such as background inorganic and organic matters and real water environment—lake water), accompanied by 100% 4-CP removal within 15 min (Figure

S18b), indicating the interference resistance of the MnN$_5$/PMS oxidation system. The k_{SA} values of all catalysts did not correlate with the contents of each surface N, C, and O species in the catalysts (Figures S19−S21 and Table S6), excluding the contribution of the nonmetallic sites to PMS activation. Thus, the atomically dispersed Mn−N moieties are the critical active sites for the outstanding performance of MnN$_5$ catalysts.

To understand the origin of the high activity of MnN$_5$, we first identified the pertinent reactive species in these two systems. Electron paramagnetic resonance (EPR) was conducted by using 5,5-dimethyl-1-pyrroline-N-oxide and TEMP as the probes of free radicals [sulfate radical (SO$_4^{·−}$) and hydroxyl radical (·OH)] and singlet oxygen (^{1}O$_2$), respectively (Figure S22). Free radical signals did not appear in the EPR spectra of the MnN$_4$/PMS and MnN$_5$/PMS systems, which was corroborated by negligible inhibition on 4-CP removal upon the addition of excessive MeOH (500 mM), a typical scavenger of free radicals (Figures 2b and S23).[8,33] The removal efficiency of 4-CP experienced a very slight decrease in the presence of 10 mM p-benzoquinone (Figure S24a), implying a negligible contribution of O$_2^{·−}$ in Mn SAC/PMS oxidation systems. Thus, the radical pathway of PMS activation could be ruled out. Although the characteristic triplet signals of TEMP-^{1}O$_2$ were observed in the EPR spectra (Figure 2c), and FFA (an ^{1}O$_2$ scavenger) mildly suppressed the 4-CP degradation, the contribution of ^{1}O$_2$ (frequently produced species with HVMO) was likely insignificant.[46] Considering the direct consumption of PMS by FFA, the degradation of 4-CP was also executed in the D$_2$O solvent due to the solvent-dependent lifetime of ^{1}O$_2$.[47] Figure S24b,c shows the minor difference between the 4-CP degradation rate in D$_2$O and H$_2$O solvents, demonstrating the negligible role of ^{1}O$_2$. In fact, the characteristic triplet signals of TEMP-^{1}O$_2$ in the MnN$_5$/PMS system were significantly lower than those in MnN$_4$/PMS (Figure 2c). Furthermore, the time-dependent evolution of ^{1}O$_2$ did not correlate with the 4-CP degradation (Figure S25), further corroborating the minor contribution of ^{1}O$_2$ to the 4-CP degradation in the Mn SAC/PMS systems.
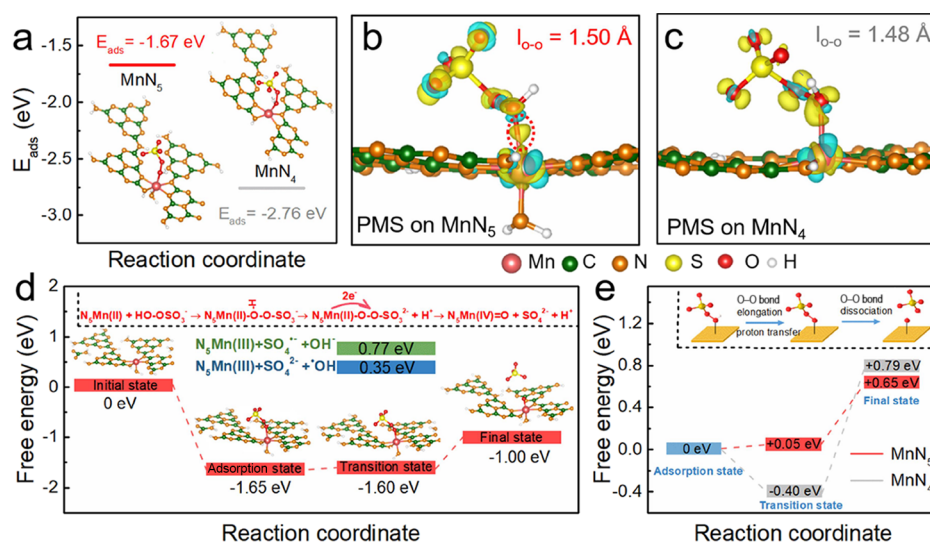
Figure 3. Theoretical calculation of PMS adsorption and activation on MnN$_5$ and MnN$_4$ catalysts. (a) Adsorption of PMS (HSO$_5^-$) on MnN$_5$ or MnN$_4$ sites of Mn SACs. The charge density difference of (b) MnN$_5$ and (c) MnN$_4$ sites after PMS adsorption. The light blue and light yellow iso-surfaces depict electron depletion and accumulation, respectively. (d) Free energy changes against reaction pathways of PMS activation at MnN$_5$ sites. (e) Comparison of free energy changes for PMS reductive activation at MnN$_5$ and MnN$_4$ sites.

Subsequently, the generation of high-valent Mn species was examined. As Mn(IV) species have been verified not to oxidize PMSO into PMSO$_2$ due to its poor reactivity of oxygen-atom transfer,[45,48] PMSO oxidation and PMSO$_2$ production failed to prove Mn(IV) species in the MnN$_5$/PMS system (Figure S26), further indicating the absence of Mn(V)=O species. In the in situ Raman spectra of PMS (Figure 2d), MnN$_5$ decreased the Raman peak intensity ratio of 1061 cm^{-1} (HSO$_5^-$) to 981 cm^{-1} (SO$_4^{2-}$) from 2.24 to 1.78, and the peak of surface-complexed PMS species at ~839 cm^{-1} appeared, corresponding to the interaction of PMS molecules with MnN$_5$. The simultaneous appearance of a new Raman peak at 746 cm^{-1} could be assigned to the stretching vibration of Mn(IV)−oxo structures,[33] suggesting that PMS molecules chemically bound to MnN$_5$ sites dissociated and transformed into Mn(IV)−oxo species.[49,50] Similar phenomena were also observed in MnN$_4$/PMS system (Figure S27), indicating that PMS activation pathways over the two catalysts were similar. Furthermore, the Mn(IV)−oxo stretching frequency (746 cm^{-1}), persisting under ambient conditions, disappeared immediately after the addition of 4-CP (Figure 2d), implying that Mn(IV)−oxo species have a strong oxidation capacity to induce a rapid electron transfer from 4-CP to Mn(IV)−oxo. Although the intensity of this peak (746 cm^{-1}) was weak due to the low Mn contents in Mn SACs, the Raman observation was in situ, and the difference among the Raman spectra was significant enough to discern the appearance and disappearance of such a peak, thus verifying the existence of the Mn(IV)−oxo species in the Mn SAC/PMS system.

As the dominant reactive species, the lifetime and reactivity of Mn(IV)−oxo for 4-CP degradation were further evaluated. The Mn(IV)−oxo-containing MnN$_5$, obtained by oxidizing MnN$_5$ with PMS in the absence of 4-CP (Text S1), were labeled as MnN$_5$-R0. The MnN$_5$-R0 stored for 1 day still could directly oxidize ~23.0% of 4-CP, resulting in higher removal than 4-CP adsorption on the fresh MnN$_5$ (~8.0%) and removal by the used catalyst (MnN$_5$-R, ~11.0%) (Figure S28a). This implies that Mn(IV)−oxo species produced from the interaction between PMS and Mn SACs had a relatively

long lifetime,[45] which makes the off-line detection of Mn(IV)−oxo feasible. The formed Mn(IV)=O on the MnN$_5$ surface was thus identified by using ABTS, which is oxidized into ABTS$^{·+}$ through single-electron transfer.[51] As seen in Figure S28b, fresh MnN$_5$ showed no reactivity with ABTS. However, in contrast to MnN$_5$-R (18%), MnN$_5$-R0 could rapidly convert ABTS (54%) into the organic cation radical of ABTS$^{·+}$, which had four characteristic adsorption peaks at 405, 640, 728, and 818 nm,[52] further corroborating the formation of Mn(IV) species on the MnN$_5$-R0 surface and its dominant role in organic oxidation. The presence of Mn(IV)−oxo species on the catalyst surface was also corroborated by XPS analyses. In the Mn 2p XPS spectra of MnN$_5$-R0, the specific satellite peak at 646.0 eV for Mn(II) in pristine MnN$_5$ vanished (Figure 2e), accompanied by a shift of the Mn 2p$_{3/2}$ peak at 641.2 eV to a higher binding energy (641.8 eV), which was normally assigned to Mn(IV).[53] Simultaneously, a new signal at 529.5 eV appeared in the O 1s spectrum (Figure 2f), corresponding to the oxygen in Mn(IV)=O moieties,[54] further proving the generation of Mn(IV)−oxo species during PMS activation. After the addition of 4-CP, the above characteristic XPS peaks of Mn(IV) and oxygen for Mn(IV)=O disappeared synchronously with the reappearance of the specific satellite peak at 646.0 eV for Mn(II). These above results excluded the contribution of free radicals, singlet oxygen, electron transfer via surface complexes, and Mn(V)−oxo and verified the existence and contribution of Mn(IV)−oxo species, thus sufficiently revealing that Mn(IV)−oxo species were the main contributors to rapid 4-CP oxidation in these Mn SAC/PMS systems.

We further quantitatively determined the contribution of possible reactive species (Mn(IV)−oxo and singlet oxygen) to 4-CP degradation by a kinetic analysis with a steady-state approximation (Text S2 and Figures S29, S30). When using FFA (5 μM) as a probe of $^1O_2$ and considering the reaction of PMS with FFA,[47] its steady-state concentrations ([$^1O_2$]$_{SS}$) in the MnN$_4$ and MnN$_5$ systems were conservatively calculated to be 1.1 × 10^{-10} and 1.7 × 10^{-11} mM, respectively (Table S7). The much lower steady-state concentration of $^1O_2$ in the
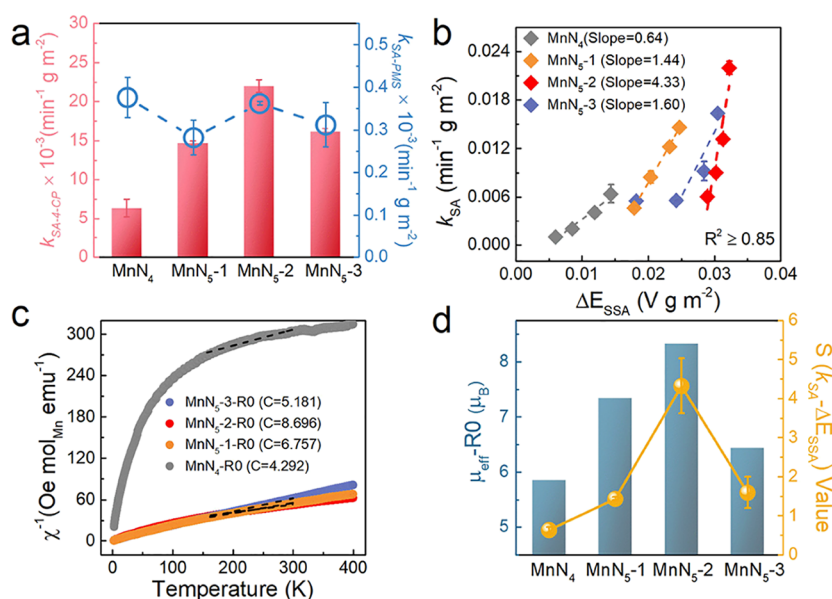
Figure 4. Significant contribution of Mn(IV)=O species and the spin state-dependent reactivity for 4-CP removal. (a) Correlation between specific PMS consumption rates ($k_{SA,PMS}$) and specific activity ($k_{SA,4-CP}$) of different Mn SACs for 4-CP degradation at $[PMS]_0$ = 1.0 mM. (b) Relationship between specific potential changes (ΔE_{SSA}) and k_{SA} for 4-CP degradation. (c) Temperature-dependent magnetic susceptibility with the Curie−Weiss fittings for the Mn SACs-R0 (the catalyst reacted with PMS excluding pollutants, that is, Mn SACs containing Mn(IV)=O). (d) Relationship between the intrinsic reactivity of Mn(IV)=O species (slope of $\Delta E_{SSA} - k_{SA}$) and μ_{eff} of Mn SACs-R0 (μ_{eff}-R0).

MnN$_5$/PMS system is consistent with the EPR results (Figure 2b). Subsequent kinetic analyses suggest that the contribution of $^1O_2$ to the 4-CP degradation in the MnN$_5$/PMS system was below 0.01%. As Mn(IV)=O species in the MnN$_5$ system accounted for nearly 100% degradation of 4-CP (Table S7), the high activity of MnN$_5$ can be attributed to either accelerated generation or enhanced reactivity of Mn(IV)=O species, which needs further investigation.

Theoretical Verification of Superior Activity of MnN$_5$ Sites for PMS Activation. We then conducted density functional theory (DFT) calculations to explore PMS adsorption and activation over Mn SACs with well-defined four- or five-coordination-number structures (MnN$_4$ and MnN$_5$). On the surface of two catalysts, PMS (HO-OSO$_3^-$) is chemically bound to the Mn sites by one peroxyl oxygen in a terminal end-on mode with large adsorption energies ($E_{ads} <$ −0.5 eV, Figure 3a) to form Mn−O(H)OSO$_3^-$, indicating that both Mn sites of MnN$_4$ and MnN$_5$ have strong PMS binding affinity.[55] After adsorption, Mn−O(H)OSO$_3^-$ is notably activated along with the significantly stretched O−O single bond from 1.39 to 1.48 Å and 1.50 Å for MnN$_4$ and MnN$_5$ sites, respectively (Table S8). The longer O−O bond on MnN$_5$ suggests a higher PMS activation capacity. The charge density difference mappings corroborate enhanced PMS activation on MnN$_5$ because more electrons are delocalized from Mn atoms to the bounded oxygen of MnN$_5$ than that of MnN$_4$ (Figure 3b,c). Subsequently, the adsorbed PMS is dissociated into an intermediate state (Mn(II)−OOSO$_3^{2-}$) by detaching a proton without an energy barrier for both MnN$_5$ and MnN$_4$ sites (Figure 3d). Then, the substantial electron donation from MnN$_5$ sites populates the peroxyl O atoms and affords a small energy barrier (+0.6 eV) for the dissociation of the O−O bond into N$_5$Mn(IV)=O (Figure 3e), in which the adsorption state was assigned as the first step. In contrast, N$_4$Mn(IV)=O formation from the intermediate state on MnN$_4$ sites is confronted with a large activation barrier (+1.19

eV) (Figure 3e). Thus, we estimated that a Mn SAC with five-nitrogen coordination is an efficient catalyst for PMS activation due to the energetically favorable generation of highly reactive N$_5$Mn(IV)=O species, which is consistent with the above experimental results.

Enhanced Reactivity of Mn(IV)−Oxo Species in the MnN$_5$/PMS System. Generally, the generation of Mn(IV)−oxo species is correlated with PMS consumption. Time-dependent PMS consumption over Mn SACs in the absence of organics was measured (Figure S31), and the specific PMS consumption rates were obtained by fitting the first-order kinetics (Figure S32), which were subsequently normalized by SSAs (Figure S33). MnN$_4$ and MnN$_5$ showed similar specific PMS consumption rates with a difference of only 3.7% at an initial PMS concentration of 1.0 mg/L (Figure 4a), suggesting that the accelerated generation of Mn(IV)−oxo species was not the main reason for the high activity of MnN$_5$ (Figures 4a and S33−S36). We then first checked the enhanced intrinsic reactivity of the N$_5$Mn(IV)=O configuration by DFT calculations. In the process of 4-CP oxidation by Mn(IV)=O species, a molecule of 4-CP (C$_6$H$_5$OCl) spontaneously adsorbed on the Mn(IV)=O sites (I → II), inducing a slight decrease of free energies for both MnN$_5$ and MnN$_4$ systems (Figure 5a). The charge density difference results indicated more electrons localizing around the oxygen atoms in the Mn(IV)=O moieties (Figure S37), which favors the formation of a transitional intermediate (III) by a strong interaction between the oxygen and the positively charged carbon atom neighboring to chlorine in 4-CP. In this rate-determining step (II → III), the oxidation of 4-CP by N$_4$Mn(IV)=O encounters a much higher energy barrier of 0.80 eV (Figure 5a). Comparatively, the oxidation barrier is only 0.32 eV at N$_5$Mn(IV)=O sites. Furthermore, the transitional configuration (III) shows that the charge transfer from the adsorbed 4-CP to N$_5$Mn(IV)=O is 0.463 e (Figure 5b), higher than that of N$_4$Mn(IV)=O (0.437 e) (Figure 5c).
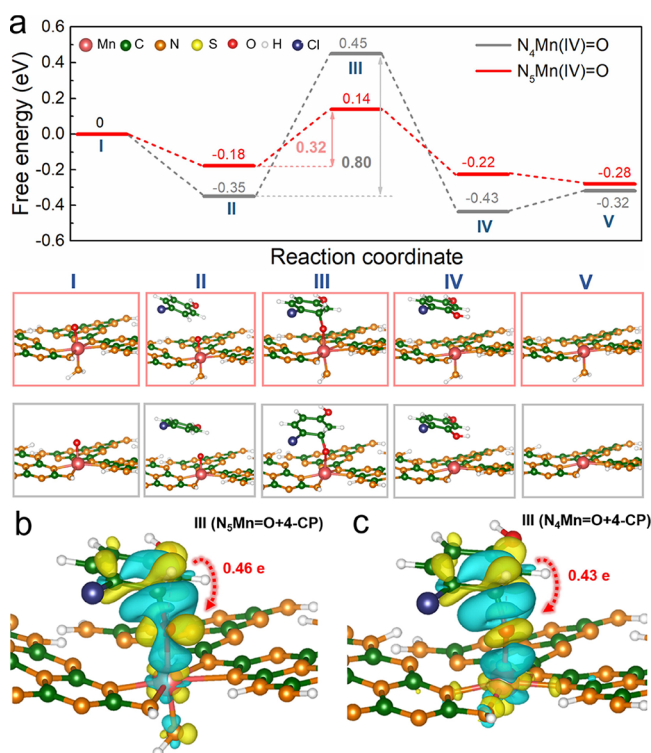
Figure 5. Theoretical calculation of 4-CP oxidation reaction over Mn(IV)=O species. (a) Comparison for free energy changes against 4-CP oxidation reaction pathways on N_5Mn(IV)=O and N_4Mn(IV)=O species. The corresponding intermediate structures are listed below the figure. The charge density differences of the optimized structure of the transition states (III) (b) N_5Mn(IV)−O−C_6H_5OCl and (c) N_4Mn(IV)−O−C_6H_5OCl. The light blue and yellow iso-surfaces depict electron depletion and accumulation, respectively.

The more favorable charge transfer and the much lower energy barriers suggest that the N_5Mn(IV)=O configuration has higher reactivity than N_4Mn(IV)=O to degrade 4-CP.

The enhanced reactivity of N_5Mn(IV)=O was corroborated by in situ open-circuit potential (OCP) tests via recording OCP values of Mn SAC electrodes with the increase of PMS dosages (Text S3).[1,33,56] The OCP values of all Mn SAC electrodes increased sharply with the addition of PMS (Figure S38), corresponding to the formation of Mn(IV)−oxo species through the heterolytic cleavage of O−O bonds.[1,57] The MnN$_5$ electrode had the highest positive OCP value in the four Mn SACs, suggesting that N_5Mn(IV)=O species have the highest oxidative capacity. We normalized the positive potential difference (ΔE) values by the SSAs of catalysts to obtain a parameter (ΔE_{SSA}). A linear positive correlation between ΔE_{SSA} and k_{SA} ($R^2 \geq 0.85$, $P < 0.05$) was obtained (Figure 4b). The slope of the correlation curve, representing the increased tendency of the organic degradation rate at the same increase of ΔE_{SSA} for Mn SACs, is an indicator of the intrinsic reactivity of Mn(IV)=O species generated in PMS activation. The slope value in the MnN$_5$/PMS system was 4.33, significantly higher than that of MnN$_4$/PMS (0.64), further proving the significantly enhanced intrinsic reactivity of N_5Mn(IV)=O species in the five-nitrogen coordinated Mn catalysts.

To further understand the basis of enhanced N_5Mn(IV)=O reactivity, we determined the magnetic property and spin state of Mn(IV)=O-containing Mn SACs (Mn SACs-R0), which

were obtained by oxidizing Mn SACs with PMS in the absence of organic substances. The magnetic susceptibilities (χ), obtained by variable-temperature (2−400 K) magnetic susceptibility (ZFC and FC) measurements at 1000 Oe (Figure S39), obey the Curie−Weiss law ($\chi = C/(T - \Theta)$), where C and Θ separately represent the Curie constant and Curie−Weiss temperature.[33] Then, the effective magnetic moment ($\mu_{eff} = \sqrt{8C}\mu_B$) was obtained by linear fitting $\chi^{-1}-T$ curves (Figure 4c).[36] Compared with fresh Mn SACs (Figure S40), the μ_{eff} values (noted as μ_{eff}-R0) for Mn SACs-R0 increased notably. All MnN$_5$-x-R0 had larger magnetic moments (μ_{eff}-R0 = 6.45−8.16 μ_B) than MnN$_4$-R0 (5.75 μ_B) (Figure 4d), suggesting that the generated N_5Mn(IV)=O species had a higher spin state than N_4Mn(IV)=O. The μ_{eff}-R0 values show a positive relationship with the intrinsic reactivity of Mn(IV)=O species (slope of $\Delta E_{SSA} - k_{SA}$) and k_{SA} values of Mn SACs (Figure 4d), implying the critical role of the spin state in the high reactivity of the generated Mn(IV)=O species. As the electron transfer from an organic molecule to the low-lying π^* orbital of metal−oxo is in concert with spin-state crossing, high-spin Mn(IV)=O species enable a relatively low energy barrier route for oxidation,[58−60] which is consistent with the above DFT analyses and OCP results (Figure 5).

The oxidation products of 4-CP were identified to explore the reactivity difference between N_5Mn(IV)=O and N_4Mn(IV)=O species (Text S4). As shown in Figure S41, the major products in Mn(IV)=O-mediated 4-CP oxidation were chlorinated oligomeric intermediates, such as dimeric substances (m/z = 219 and 253) and trimeric products (m/z = 345 and 379). The postulated transformation pathways of 4-CP by the Mn(IV)=O-mediated oxidation process are presented in Figure 6a. Chlorophenoxyonium ions produced by 4-CP oxidation would form positively charged phenolic
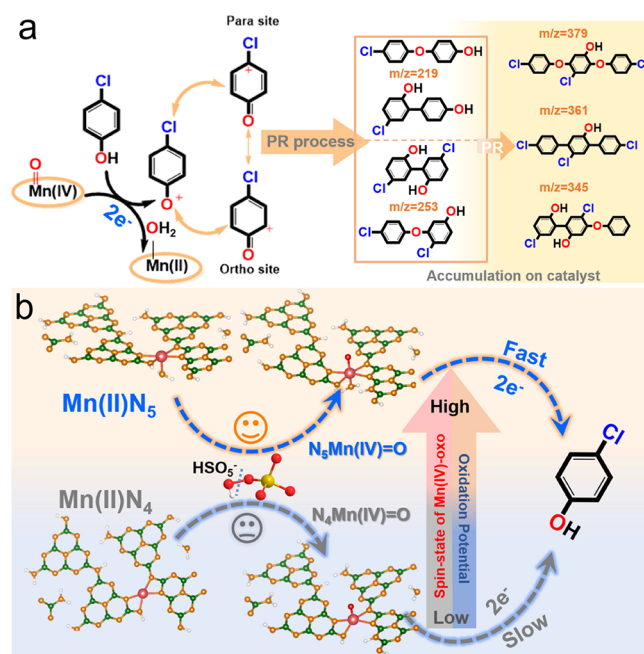

Figure 6. Evolution oxidation process of 4-CP in Mn(IV)-mediated PMS activation. (a) Proposed reaction pathways of 4-CP in the Mn(IV)=O-mediated oxidation process. (b) Schematic illustration for the Mn(IV)−oxo-based PMS activation mechanism.

hydroxyl groups at *para-* and *ortho-*sites via instantaneous resonance transfer;[61,62] then these intermediates spontaneously undergo polymerization (PR) to generate chlorinated oligomeric products (Figure S41). The MnN$_5$/PMS system (Figure S41b) produced more trimeric (m/z = 345 and 379) and dimeric substances (m/z = 253) than MnN$_4$/PMS (Figure S41a), suggesting the faster 2e$^-$-transfer between N$_5$Mn(IV)=O and 4-CP, which is consistent with the high reactivity of N$_5$Mn(IV)=O. Based on the above DFT and experimental results, in comparison to MnN$_4$, MnN$_5$ enables more efficient PMS activation to generate high-spin N$_5$Mn(IV)=O species with a stronger oxidation capacity, resulting in the faster 2e$^-$-oxidation of organic pollutants (Figure 6b). In conclusion, Mn(IV)=O species formed on the Mn SAC surface could serve as electron acceptors, leading to the PR of 4-CP and generating no residual byproducts that could be released to the aqueous environment. Thus, this Mn(IV)=O-mediated heterogeneous PMS activation system has the potential to remove phenolic pollutants and recover polymerized organic residuals from water.

Environmental Implications. Five-nitrogen coordinated Mn SACs have been overlooked for efficient persulfate activation during the treatment of wastewater contaminated by recalcitrant organic compounds and for groundwater remediation. This work addresses a fundamental knowledge gap in coordination chemistry to boost PMS activation and highlights the critical role of five-nitrogen coordinated Mn SACs to form highly reactive Mn(IV)−oxo species that significantly enhance such AOPs. Specifically, during PMS activation, Mn(II) sites on the catalysts are spontaneously oxidized into reactive Mn(IV)−oxo species, whose reactivity strongly depends on the coordination number of nitrogen atoms. Compared to MnN$_4$, MnN$_5$ enables more efficient PMS activation to generate N$_5$Mn(IV)−oxo species with higher reactivity, which is facilitated by the higher spin state of Mn(IV)−oxo species under five-nitrogen coordinated conditions. Accordingly, the rapid two-electron transfer from target organics to the generated N$_5$Mn(IV)−oxo species promotes organic oxidation with high PMS activation efficiency. These mechanistic insights indicate that the activity of SACs in HVMO-mediated PMS activation depends greatly on the coordination numbers, which control the reactivity of HVMO species. Overall, this work provides a strategy to develop SACs with high nitrogen coordination numbers, which enhance PMS-based AOPs, and encourages exploration of other transitional metals with high nitrogen coordination numbers to develop next-generation environmental catalysts that enhance HVMO-mediated PMS-based AOPs.

ASSOCIATED CONTENT

Supporting Information

The Supporting Information is available free of charge at https://pubs.acs.org/doi/10.1021/acs.est.2c08836.

> Characterization; degradation of 4-CP and its reaction kinetics in different PMS activation systems; adsorption of 4-CP; comparison of the k_{SA} of different organics; cycle tests; correlation between k_{SA} and N, C, and O species; identification and quantifying the contribution of ROS; preparation of pre-oxidized Mn SACs (i.e., MnN$_5$-R0) and their oxidation of 4-CP; PMS decomposition; comparison of k_{SA-PMS} values and their relationship with $k_{SA-4-CP}$ values; DFT results; electro-

chemical measurement; and identification of degradation intermediates of 4-CP (PDF)

AUTHOR INFORMATION

Corresponding Authors

Mingce Long − *School of Environmental Science and Engineering, Key Laboratory for Thin Film and Microfabrication of the Ministry of Education, Shanghai Jiao Tong University, Shanghai 200240, China;* orcid.org/0000-0002-5168-8330; Email: long_mc@sjtu.edu.cn

Lizhi Zhang − *School of Environmental Science and Engineering, Key Laboratory for Thin Film and Microfabrication of the Ministry of Education, Shanghai Jiao Tong University, Shanghai 200240, China;* Email: zhanglizhi@sjtu.edu.cn

Authors

Jie Miao − *School of Environmental Science and Engineering, Key Laboratory for Thin Film and Microfabrication of the Ministry of Education, Shanghai Jiao Tong University, Shanghai 200240, China*

Jian Song − *School of Environmental Science and Engineering, Key Laboratory for Thin Film and Microfabrication of the Ministry of Education, Shanghai Jiao Tong University, Shanghai 200240, China*

Junyu Lang − *School of Physical Science and Technology, Shanghai Tech University, Shanghai 201210, China*

Yuan Zhu − *School of Chemistry and Chemical Engineering, Queen's University Belfast, Belfast BT7 1NN, U.K.*

Jie Dai − *School of Environmental Science and Engineering, Key Laboratory for Thin Film and Microfabrication of the Ministry of Education, Shanghai Jiao Tong University, Shanghai 200240, China*

Yan Wei − *School of Environmental Science and Engineering, Key Laboratory for Thin Film and Microfabrication of the Ministry of Education, Shanghai Jiao Tong University, Shanghai 200240, China*

Zongping Shao − *WA School of Mines: Minerals, Energy and Chemical Engineering, Curtin University, Perth, Western Australia 6845, Australia;* orcid.org/0000-0002-4538-4218

Baoxue Zhou − *School of Environmental Science and Engineering, Key Laboratory for Thin Film and Microfabrication of the Ministry of Education, Shanghai Jiao Tong University, Shanghai 200240, China;* orcid.org/0000-0001-9691-3119

Pedro J. J. Alvarez − *Department of Civil and Environmental Engineering, Rice University, Houston, Texas 77005, United States;* orcid.org/0000-0002-6725-7199

Complete contact information is available at:
https://pubs.acs.org/10.1021/acs.est.2c08836

Notes

The authors declare no competing financial interest.

Center for High Performance Computing at Shanghai Jiao Tong University.

■ REFERENCES

(1) Zhou, X.; Ke, M. K.; Huang, G. X.; Chen, C.; Chen, W.; Liang, K.; Qu, Y.; Yang, J.; Wang, Y.; Li, F.; Yu, H. Q.; Wu, Y. Identification of Fenton-like active Cu sites by heteroatom modulation of electronic density. *Proc. Natl. Acad. Sci. U. S. A.* **2022**, *119*, No. e2119492119.

(2) Alvarez, P. J. J.; Chan, C. K.; Elimelech, M.; Halas, N. J.; Villagrán, D. Emerging opportunities for nanotechnology to enhance water security. *Nat. Nanotechnol.* **2018**, *13*, 634−641.

(3) Guo, Z. Y.; Li, C. X.; Gao, M.; Han, X.; Zhang, Y. J.; Zhang, W. J.; Li, W. W. Mn-O covalency governs the intrinsic activity of Co-Mn spinel oxides for boosted peroxymonosulfate activation. *Angew. Chem., Int. Ed.* **2021**, *60*, 274−280.

(4) Chen, Y.; Zhang, G.; Liu, H.; Qu, J. Confining free radicals in close vicinity to contaminants enables ultrafast Fenton-like processes in the interspacing of MoS₂ membranes. *Angew. Chem., Int. Ed.* **2019**, *58*, 8134−8138.

(5) Anipsitakis, G. P.; Dionysiou, D. D. Radical generation by the interaction of transition metals with common oxidants. *Environ. Sci. Technol.* **2004**, *38*, 3705−3712.

(6) Huang, J.; Zhang, H. Mn-based catalysts for sulfate radical-based advanced oxidation processes: A review. *Environ. Int.* **2019**, *133*, No. 105141.

(7) Wu, H.; Xu, X.; Shi, L.; Yin, Y.; Zhang, L.-C.; Wu, Z.; Duan, X.; Wang, S.; Sun, H. Manganese oxide integrated catalytic ceramic membrane for degradation of organic pollutants using sulfate radicals. *Water Res.* **2019**, *167*, No. 115110.

(8) Qian, K.; Chen, H.; Li, W.; Ao, Z.; Wu, Y.-n.; Guan, X. Single-atom Fe catalyst outperforms its homogeneous counterpart for activating peroxymonosulfate to achieve effective degradation of organic contaminants. *Environ. Sci. Technol.* **2021**, *55*, 7034−7043.

(9) Oh, W.-D.; Dong, Z.; Lim, T.-T. Generation of sulfate radical through heterogeneous catalysis for organic contaminants removal: Current development, challenges and prospects. *Appl. Catal., B* **2016**, *194*, 169−201.

(10) Wang, Z.; Qiu, W.; Pang, S. Y.; Guo, Q.; Guan, C.; Jiang, J. Aqueous iron(IV)-oxo complex: An emerging powerful reactive oxidant formed by iron(II)-based advanced oxidation processes for oxidative water treatment. *Environ. Sci. Technol.* **2022**, *56*, 1492−1509.

(11) Pestovsky, O.; Bakac, A. Reactivity of aqueous Fe(IV) in hydride and hydrogen atom transfer reactions. *J. Am. Chem. Soc.* **2004**, *126*, 13757−13764.

(12) Liu, B.; Guo, W.; Jia, W.; Wang, H.; Si, Q.; Zhao, Q.; Luo, H.; Jiang, J.; Ren, N. Novel nonradical oxidation of sulfonamide antibiotics with Co(II)-doped g-C₃N₄-activated peracetic acid: Role of high-valent cobalt-oxo species. *Environ. Sci. Technol.* **2021**, *55*, 12640−12651.

(13) Zhou, C.; Bai, J.; Zhang, Y.; Li, J.; Li, Z.; Jiang, P.; Fang, F.; Zhou, M.; Mei, X.; Zhou, B. Novel 3D Pd-Cu(OH)₂/CF cathode for rapid reduction of nitrate-N and simultaneous total nitrogen removal from wastewater. *J. Hazard. Mater.* **2021**, *401*, No. 123232.

(14) Wang, Z.; Jiang, J.; Pang, S.; Zhou, Y.; Guan, C.; Gao, Y.; Li, J.; Yang, Y.; Qu, W.; Jiang, C. Is sulfate radical really generated from peroxydisulfate activated by iron(II) for environmental decontamination? *Environ. Sci. Technol.* **2018**, *52*, 11276−11284.

(15) Zong, Y.; Guan, X.; Xu, J.; Feng, Y.; Mao, Y.; Xu, L.; Chu, H.; Wu, D. Unraveling the overlooked involvement of high-valent cobalt-oxo species generated from the cobalt(II)-activated peroxymonosulfate process. *Environ. Sci. Technol.* **2020**, *54*, 16231−16239.

(16) Wang, L.; Xu, H.; Jiang, N.; Wang, Z.; Jiang, J.; Zhang, T. Trace cupric species triggered decomposition of peroxymonosulfate and degradation of organic pollutants: Cu(III) being the primary and selective intermediate oxidant. *Environ. Sci. Technol.* **2020**, *54*, 4686−4694.

(17) Wang, Z.; Qiu, W.; Pang, S.-Y.; Zhou, Y.; Gao, Y.; Guan, C.; Jiang, J. Further understanding the involvement of Fe(IV) in peroxydisulfate and peroxymonosulfate activation by Fe(II) for oxidative water treatment. *Chem. Eng. J.* **2019**, *371*, 842−847.

(18) Wei, Y.; Miao, J.; Ge, J.; Lang, J.; Yu, C.; Zhang, L.; Alvarez, P. J. J.; Long, M. Ultrahigh peroxymonosulfate utilization efficiency over CuO nanosheets via heterogeneous Cu(III) formation and preferential electron transfer during degradation of phenols. *Environ. Sci. Technol.* **2022**, *56*, 8984−8992.

(19) Wei, J.; Xiong, Z.; Ao, M.; Guo, Z.; Zhang, J.; Lai, B.; Song, Y. Selective degradation of sulfamethoxazole by N-doped iron-based carbon activated peroxymonosulfate: Collaboration of singlet oxygen and high-valent iron-oxo species. *Sep. Purif. Technol.* **2022**, *297*, No. 121379.

(20) Mi, X.; Wang, P.; Xu, S.; Su, L.; Zhong, H.; Wang, H.; Li, Y.; Zhan, S. Almost 100% peroxymonosulfate conversion to singlet oxygen on single-atom CoN₂₊₂ sites. *Angew. Chem., Int. Ed.* **2020**, *133*, 4638−4643.

(21) Zhang, L. S.; Jiang, X. H.; Zhong, Z. A.; Tian, L.; Sun, Q.; Cui, Y. T.; Lu, X.; Zou, J. P.; Luo, S. L. Carbon nitride supported high-loading Fe single-atom catalyst for activation of peroxymonosulfate to generate ¹O₂ with 100% selectivity. *Angew. Chem., Int. Ed.* **2021**, *60*, 21751−21755.

(22) Shang, Y.; Xu, X.; Gao, B.; Wang, S.; Duan, X. Single-atom catalysis in advanced oxidation processes for environmental remediation. *Chem. Soc. Rev.* **2021**, *50*, 5281−5322.

(23) Wu, X.; Kim, J.-H. Outlook on single atom catalysts for persulfate-based advanced oxidation. *ACS ES&T Eng.* **2022**, *2*, 1776−1796.

(24) Zhang, B.; Li, X.; Akiyama, K.; Bingham, P. A.; Kubuki, S. Elucidating the mechanistic origin of a spin state-dependent FeNₓ-C catalyst toward organic contaminant oxidation via peroxymonosulfate activation. *Environ. Sci. Technol.* **2022**, *56*, 1321−1330.

(25) Li, F.; Lu, Z.; Li, T.; Zhang, P.; Hu, C. Origin of the excellent activity and selectivity of a single-atom copper catalyst with unsaturated Cu-N₂ sites via peroxydisulfate activation: Cu(III) as a dominant oxidizing species. *Environ. Sci. Technol.* **2022**, *56*, 8765−8775.

(26) Wu, X.; Zhang, H.; Zuo, S.; Dong, J.; Li, Y.; Zhang, J.; Han, Y. Engineering the coordination sphere of isolated active sites to explore the intrinsic activity in single-atom catalysts. *Nano-Micro Lett.* **2021**, *13*, 136.

(27) Liang, X.; Wang, D.; Zhao, Z.; Li, T.; Gao, Y.; Hu, C. Coordination number dependent catalytic activity of single-atom cobalt catalysts for Fenton-like reaction. *Adv. Funct. Mater.* **2022**, *32*, No. 2203001.

(28) Guo, M.; Seo, M. S.; Lee, Y. M.; Fukuzumi, S.; Nam, W. Highly reactive manganese(IV)-oxo porphyrins showing temperature-dependent reversed electronic effect in C-H bond activation reactions. *J. Am. Chem. Soc.* **2019**, *141*, 12187−12191.

(29) Sharma, N.; Jung, J.; Ohkubo, K.; Lee, Y. M.; El-Khouly, M. E.; Nam, W.; Fukuzumi, S. Long-lived photoexcited state of a Mn(IV)-Oxo complex binding scandium ions that is capable of hydroxylating benzene. *J. Am. Chem. Soc.* **2018**, *140*, 8405−8409.

(30) Guo, M.; Zhang, J.; Zhang, L.; Lee, Y. M.; Fukuzumi, S.; Nam, W. Enthalpy-entropy compensation effect in oxidation reactions by manganese(IV)-oxo porphyrins and nonheme iron(IV)-oxo models. *J. Am. Chem. Soc.* **2021**, *143*, 18559−18570.

(31) Zhu, C.; Nie, Y.; Cun, F.; Wang, Y.; Tian, Z.; Liu, F. Two-step pyrolysis to anchor ultrahigh-density single-atom FeN₅ sites on carbon nitride for efficient Fenton-like catalysis near 0 °C. *Appl. Catal., B* **2022**, *319*, No. 121900.

(32) Zhang, H. C.; Cui, P. X.; Xie, D. H.; Wang, Y. J.; Wang, P.; Sheng, G. P. Axial N ligand-modulated ultrahigh activity and selectivity hyperoxide activation over single-atoms nanozymes. *Adv. Sci.* **2022**, *10*, No. e2205681.

(33) Miao, J.; Zhu, Y.; Lang, J.; Zhang, J.; Cheng, S.; Zhou, B.; Zhang, L.; Alvarez, P. J. J.; Long, M. Spin-state-dependent peroxymonosulfate activation of single-atom M-N moieties via a radical-free pathway. *ACS Catal.* **2021**, *11*, 9569−9577.

(34) Guo, Z.; Xie, Y.; Xiao, J.; Zhao, Z. J.; Wang, Y.; Xu, Z.; Zhang, Y.; Yin, L.; Cao, H.; Gong, J. Single-atom Mn-N_4 site-catalyzed peroxone reaction for the efficient production of hydroxyl radicals in an acidic solution. *J. Am. Chem. Soc.* **2019**, *141*, 12005−12010.

(35) Wu, X.; Gao, D.; Wang, P.; Yu, H.; Yu, J. NH_4Cl-induced low-temperature formation of nitrogen-rich g-C_3N_4 nanosheets with improved photocatalytic hydrogen evolution. *Carbon* **2019**, *153*, 757−766.

(36) Sun, S.; Shen, G.; Jiang, J.; Mi, W.; Liu, X.; Pan, L.; Zhang, X.; Zou, J.-J. Boosting oxygen evolution kinetics by Mn-N-C motifs with tunable spin state for highly efficient solar-driven water splitting. *Adv. Energy Mater.* **2019**, *9*, No. 1901505.

(37) Yang, T.; Mao, X.; Zhang, Y.; Wu, X.; Wang, L.; Chu, M.; Pao, C.-W.; Yang, S.; Xu, Y.; Huang, X. Coordination tailoring of Cu single sites on C_3N_4 realizes selective CO_2 hydrogenation at low temperature. *Nat. Commun.* **2021**, *12*, 6022.

(38) Masa, J.; Xia, W.; Sinev, I.; Zhao, A.; Sun, Z.; Grützke, S.; Weide, P.; Muhler, M.; Schuhmann, W. Mn_xO_y/NC and Co_xO_y/NC nanoparticles embedded in a nitrogen-doped carbon matrix for high-performance bifunctional oxygen electrodes. *Angew. Chem., Int. Ed.* **2014**, *53*, 8508−8512.

(39) Cao, Y.; Chen, S.; Luo, Q.; Yan, H.; Lin, Y.; Liu, W.; Cao, L.; Lu, J.; Yang, J.; Yao, T.; Wei, S. Atomic-level insight into optimizing the hydrogen evolution pathway over a Co_1N_4 single-site photo-catalyst. *Angew. Chem., Int. Ed.* **2017**, *56*, 12191−12196.

(40) Gao, Y.; Wu, T.; Yang, C.; Ma, C.; Zhao, Z.; Wu, Z.; Cao, S.; Geng, W.; Wang, Y.; Yao, Y.; Zhang, Y.; Cheng, C. Activity trends and mechanisms in peroxymonosulfate-assisted catalytic production of singlet oxygen over atomic metal-N-C catalysts. *Angew. Chem., Int. Ed.* **2021**, *60*, 22513−22521.

(41) Wang, Y.; Sun, H.; Ang, H. M.; Tadé, M. O.; Wang, S. Facile synthesis of hierarchically structured magnetic MnO_2/$ZnFe_2O_4$ hybrid materials and their performance in heterogeneous activation of peroxymonosulfate. *ACS Appl. Mater. Interfaces* **2014**, *6*, 19914−19923.

(42) Huang, Y.; Tian, X.; Nie, Y.; Yang, C.; Wang, Y. Enhanced peroxymonosulfate activation for phenol degradation over MnO_2 at pH 3.5-9.0 via Cu(II) substitution. *J. Hazard. Mater.* **2018**, *360*, 303−310.

(43) Gao, B.; Zhu, S.; Gu, J.; Liu, Y.; Yi, X.; Zhou, H. Superoxide radical mediated Mn(III) formation is the key process in the activation of peroxymonosulfate (PMS) by Mn-incorporated bacterial-derived biochar. *J. Hazard. Mater.* **2022**, *431*, No. 128549.

(44) Ke, M. K.; Huang, G. X.; Mei, S. C.; Wang, Z. H.; Zhang, Y. J.; Hua, T. W.; Zheng, L. R.; Yu, H. Q. Interface-promoted direct oxidation of p-arsanilic acid and removal of total arsenic by the coupling of peroxymonosulfate and Mn-Fe-mixed oxide. *Environ. Sci. Technol.* **2021**, *55*, 7063−7071.

(45) Li, H.; Yuan, N.; Qian, J.; Pan, B. Mn_2O_3 as an electron shuttle between peroxymonosulfate and organic pollutants: The dominant role of surface reactive Mn(IV) species. *Environ. Sci. Technol.* **2022**, *56*, 4498−4506.

(46) Yang, Y.; Banerjee, G.; Brudvig, G. W.; Kim, J.-H.; Pignatello, J. J. Oxidation of organic compounds in water by unactivated peroxymonosulfate. *Environ. Sci. Technol.* **2018**, *52*, 5911−5919.

(47) Lee, J.; von Gunten, U.; Kim, J. H. Persulfate-based advanced oxidation: Critical assessment of opportunities and roadblocks. *Environ. Sci. Technol.* **2020**, *54*, 3064−3081.

(48) Neu, H. M.; Baglia, R. A.; Goldberg, D. P. A balancing act: Stability versus reactivity of Mn-O complexes. *Acc. Chem. Res.* **2015**, *48*, 2754−2764.

(49) Park, S.; Jin, K.; Lim, H. K.; Kim, J.; Cho, K. H.; Choi, S.; Seo, H.; Lee, M. Y.; Lee, Y. H.; Yoon, S.; Kim, M.; Kim, H.; Kim, S. H.; Nam, K. T. Spectroscopic capture of a low-spin Mn(IV)-oxo species in Ni-Mn_3O_4 nanoparticles during water oxidation catalysis. *Nat. Commun.* **2020**, *11*, 5230.

(50) Jin, K.; Seo, H.; Hayashi, T.; Balamurugan, M.; Jeong, D.; Go, Y. K.; Hong, J. S.; Cho, K. H.; Kakizaki, H.; Bonnet-Mercier, N.; Kim, M. G.; Kim, S. H.; Nakamura, R.; Nam, K. T. Mechanistic investigation of water oxidation catalyzed by uniform, assembled MnO nanoparticles. *J. Am. Chem. Soc.* **2017**, *139*, 2277−2285.

(51) Yin, G. Understanding the oxidative relationships of the metal oxo, hydroxo, and hydroperoxide intermediates with manganese(IV) complexes having bridged cyclams: correlation of the physicochemical properties with reactivity. *Acc. Chem. Res.* **2013**, *46*, 483−492.

(52) Huang, Y.; Zou, J.; Lin, J.; Yang, H.; Wang, M.; Li, J.; Cao, W.; Yuan, B.; Ma, J. ABTS as both activator and electron shuttle to activate persulfate for diclofenac degradation: Formation and contributions of ABTS$^{•+}$, $SO_4^{•-}$, and $^•OH$. *Environ. Sci. Technol.* **2022**, 2c04318.

(53) Nesbitt, H. W.; Banerjee, D. Interpretation of XPS Mn 2p spectra of Mn oxyhydroxides and constraints on the mechanism of MnO_2 precipitation. *Am. Mineral.* **1998**, *83*, 305−315.

(54) Stranick, M. A. MnO_2 by XPS. *Surf. Sci. Spectra* **1999**, *6*, 31−38.

(55) Zhang, P.; Yang, Y.; Duan, X.; Liu, Y.; Wang, S. Density functional theory calculations for insight into the heterocatalyst reactivity and mechanism in persulfate-based advanced oxidation reactions. *ACS Catal.* **2021**, *11*, 11129−11159.

(56) Wang, Z.; Almatrafi, E.; Wang, H.; Qin, H.; Wang, W.; Du, L.; Chen, S.; Zeng, G.; Xu, P. Cobalt single atoms anchored on oxygen-doped tubular carbon nitride for efficient peroxymonosulfate activation: Simultaneous coordination structure and morphology modulation. *Angew. Chem., Int. Ed.* **2022**, No. e202202338.

(57) Wang, Y.; Xia, H.; Sun, K.; Wu, S.; Lu, W.; Xu, J.; Li, N.; Pei, K.; Zhu, Z.; Chen, W. Insights into the generation of high-valent copper-oxo species in ligand-modulated catalytic system for oxidizing organic pollutants. *Chem. Eng. J.* **2016**, *304*, 1000−1008.

(58) Larson, V. A.; Battistella, B.; Ray, K.; Lehnert, N.; Nam, W. Iron and manganese oxo complexes, oxo wall and beyond. *Nat. Rev. Chem.* **2020**, *4*, 404−419.

(59) Li, X.-X.; Guo, M.; Qiu, B.; Cho, K.-B.; Sun, W.; Nam, W. High-spin Mn(V)-oxo intermediate in nonheme manganese complex-catalyzed alkane hydroxylation reaction: Experimental and theoretical approach. *Inorg. Chem.* **2019**, *58*, 14842−14852.

(60) Hirao, H.; Kumar, D.; Que, L.; Shaik, S. Two-state reactivity in alkane hydroxylation by non-heme iron-oxo complexes. *J. Am. Chem. Soc.* **2006**, *128*, 8590−8606.

(61) Zhang, Y.-J.; Huang, G.-X.; Winter, L. R.; Chen, J.-J.; Tian, L.; Mei, S.-C.; Zhang, Z.; Chen, F.; Guo, Z.-Y.; Ji, R.; You, Y.-Z.; Li, W.-W.; Liu, X.-W.; Yu, H.-Q.; Elimelech, M. Simultaneous nanocatalytic surface activation of pollutants and oxidants for highly efficient water decontamination. *Nat. Commun.* **2022**, *13*, 3005.

(62) Vigalok, A.; Rybtchinski, B.; Gozin, Y.; Koblenz, T. S.; Ben-David, Y.; Rozenberg, H.; Milstein, D. Metal-stabilized phenoxonium cation. *J. Am. Chem. Soc.* **2003**, *125*, 15692−15693.